remote sensing

MDPI

Article

Satellite-Derived Indicators of Drought Severity and Water Storage in Estuarine Reservoirs: A Case Study of Qingcaosha Reservoir, China

Rui Yuan [1], Ruiyang Xu [1], Hezhenjia Zhang [1], Cheng Qiu [2] and Jianrong Zhu [3,*]

[1] School of Ocean Science and Engineering, Shanghai Maritime University, 1550 Haigang Ave., Shanghai 201306, China; yuanrui@shmtu.edu.cn (R.Y.); 202230410132@stu.shmtu.edu.cn (R.X.); 201810413023@stu.shmtu.edu.cn (H.Z.)
[2] Shanghai Marine Monitoring and Forecasting Center, Shanghai 200062, China; qiucheng@smmfc.com
[3] State Key Laboratory of Estuarine and Coastal Research, East China Normal University, Shanghai 200241, China
* Correspondence: jrzhu@sklec.ecnu.edu.cn; Tel.: +86-021-54836024

Abstract: Estuarine reservoirs are critical for freshwater supply and security, especially for regions facing water scarcity challenges due to climate change and population growth. Conventional methods for assessing drought severity or monitoring reservoir water level and storage are often limited by data availability, accessibility and quality. We present an approach for monitoring estuarine reservoir water levels, storage and extreme drought via satellite remote sensing and waterline detection. Based on the CoastSat algorithm, Landsat-8 and Sentinel-2 images from 2013 to 2022 were adopted to extract the waterline of Qingcaosha Reservoir, the largest estuarine reservoir in the world and a key source of freshwater for Shanghai, China. This study confirmed the accuracy of the satellite-extracted results through two main methods: (1) calculating the angle of the central shoal slope in the reservoir using the extracted waterline data and measured water levels and (2) inverting the time series of water levels for comparison with measured data. The correlation coefficient of the estimated water level reached ~0.86, and the root mean square error (RMSE) of the estimated shoal slope was ~0.2°, indicating that the approach had high accuracy and reliability. We analyzed the temporal and spatial patterns of waterline changes and identified two dates (21 February 2014 and 15 October 2022) when the reservoir reached the lowest water levels, coinciding with periods of severe saltwater intrusions in the estuary. The extreme drought occurrences in the Qingcaosha Reservoir were firstly documented through the utilization of remote sensing data. The results also indicate a strong resilience of the Qingcaosha Reservoir and demonstrate that the feasibility and utility of using satellite remote sensing and waterline detection for estuarine reservoir storage can provide timely and accurate information for water resource assessment, management and planning.

Keywords: estuarine reservoir; extreme low water level events; waterline extraction; water resource; saltwater intrusion

Citation: Yuan, R.; Xu, R.; Zhang, H.; Qiu, C.; Zhu, J. Satellite-Derived Indicators of Drought Severity and Water Storage in Estuarine Reservoirs: A Case Study of Qingcaosha Reservoir, China. *Remote Sens.* **2024**, *16*, 980. https://doi.org/10.3390/rs16060980

Academic Editors: Gabriel Senay and Won-Ho Nam

Received: 8 January 2024
Revised: 14 February 2024
Accepted: 6 March 2024
Published: 11 March 2024

1. Introduction

Estuarine reservoirs are particularly important for estuary regions, where large rivers meet the sea and form complex and productive ecosystems. Estuary regions are often densely populated and highly developed, as they provide abundant natural resources (e.g., water, food and tidal energy) and strategic advantages (e.g., transportation and trade). However, they are also facing multiple challenges and threats, such as sea level rise [1], saltwater intrusion [2], flooding [3], drought [4] and pollution [5]. Estuarine reservoirs can play a vital role in enhancing the resilience and sustainability of estuary regions by regulating the freshwater–saltwater balance, buffering the impacts of extreme events, storing and supplying water for various uses, generating renewable energy and maintaining ecological functions and services [6,7]. Therefore, understanding and managing the water

resources of estuarine reservoirs is crucial for the well-being and prosperity of estuary regions and their inhabitants.

Typical droughts include meteorological drought, agricultural drought, hydrological drought and socio-economic drought [8]. This study concentrates on hydrological reservoir drought, which could be considered as a specific condition characterized by significantly reduced water levels within a reservoir due to prolonged periods of insufficient freshwater inflow [9]. Estuarine reservoir storage might be unstable due to continuous saltwater intrusion occurring during the dry season, when the river discharge is low or the oceanic dynamic condition is anomalously strong [10–12]. However, saltwater intrusions also occur, even during flood seasons under the influences of abnormally extreme drought [13,14] and typhoons [15,16]. For instance, 2022 was reported as a year of drought [17], when continuous drought occurred in the Changjiang River Basin. Figure 1 shows the dramatic decrease in river discharge in the flood season of 2022. Through comparison with continuous data collected since 1950, the historical extreme drought event was effectively illustrated. The monitored river discharge was obtained from Datong Station, which is located approximately 624 km from the mouth of the Changjiang River and serves as the tidal limit. It plays an important role in the observation of water changes in the Changjiang River system [18,19]. The river water level decrease was also visible in the satellite images, and the obvious increase in the island area is shown in Figure 1c,d. Data of river discharge into the sea are obtained by Datong station, and its water level serves as important reference data for flood and drought defense downstream of the Changjiang River [20].

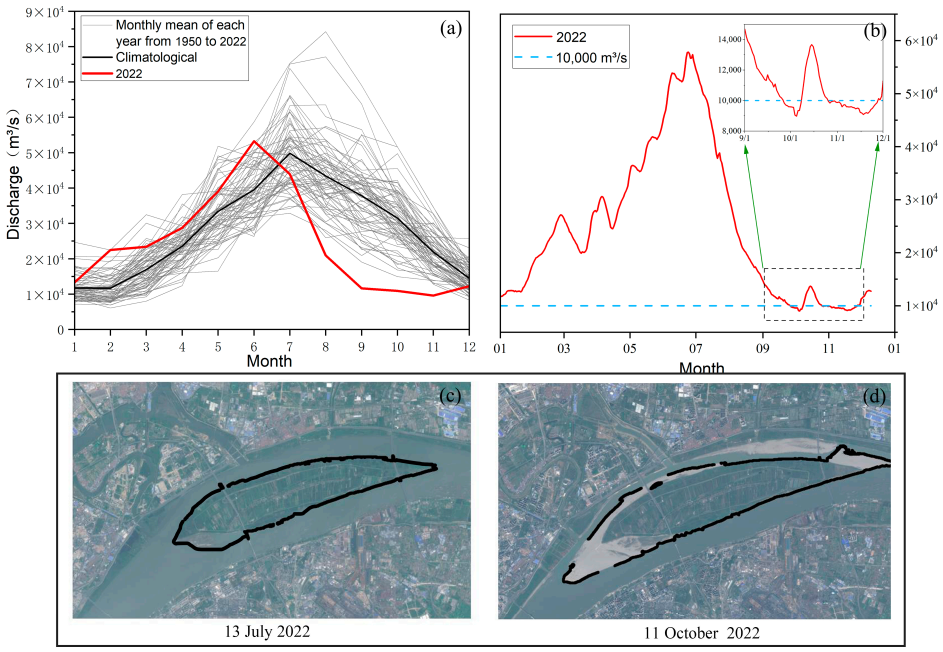

Figure 1. (**a**) Monthly mean river discharge variations at Datong station from 1950 to 2022. The red solid line represents the data for 2022, the black solid line is the monthly mean river discharge from 1950 to 2022 and the gray solid line is the monthly average in each year. The discharge data were obtained from the Anhui Water Information at http://slt.ah.gov.cn/ (accessed on 10 November 2022). (**b**) Daily average river discharge variations at Datong station in 2022. The blue dashed line represents 10,000 m^3/s. (**c**,**d**) represent the original satellite images of Tianxingzhou in the upper reaches of the Changjiang River; the solid black line represents the waterline calculated by CoastSat. The satellite image source was Sentinel-2.

The statistical results indicate that the water availability of the Changjiang River in the summer and autumn of 2022 was very low. The river discharge at Datong station dropped sharply from July to November in 2022, with it reaching its lowest level in the past 70 years. Furthermore, the daily average river discharge shows a cliff-like decrease after 24 June, reaching 8982 m^3/s on 5 October, with a decrease rate of 84.47%, which is less than one-third of the daily average river discharge during the same period. In August, the monthly mean river discharge from 1950 to 2022 was 44,900 m^3/s, but on 15 August in 2022, it was only 20,300 m^3/s, which is more than 50% lower than the monthly mean value. In late September, the daily average river discharge dropped below 10,000 m^3/s, which is 70% lower than the historical average value. In this case, estuarine reservoirs faced a significant risk of saltwater intrusion and a critical water supply situation. Therefore, monitoring the changes in relevant indicators of estuarine reservoirs is crucial for effective water resource management and sustainable development [21]. Due to their unique locations and limited data availability, monitoring and evaluating the water resources of estuarine reservoirs have always been challenging tasks.

Compared with estuarine reservoirs, the instability of water storage in river extent, inland reservoirs and lakes are common and widely studied [22–25]. Satellite remote sensing technology is a novel monitoring method that significantly enhances efficiency [26]. The continuous development of remote sensing technology has also made it applicable to water resource management and available to a wider user base through technological innovation [22]. Currently, various approaches to monitoring water bodies involve the effective utilization of satellite remote sensing at varying resolutions to detect and analyze them, thus allowing for the acquisition of frequent and consistent spatial data over a large area, which is crucial for monitoring changes in water resources. The use of different water indices to distinguish between water and land is important. Optical satellite images processed by the normalized difference water index (NDWI) are used for mapping urban surface water extraction and have achieved good accuracy [27]. Modifications have been made to the near-infrared band used in the NDWI, and the improved modified normalized difference water index (MNDWI) is more suitable for water extraction in urban areas [28]. In early studies on reservoir monitoring, satellite remote sensing technology was employed to validate the strong correlation between the MODIS-based data (including water level, surface area and storage volume) of 34 major reservoirs globally and corresponding observations. As a result, a comprehensive dataset of reservoir storage at a global scale was generated [29]. Thereafter, a dataset for 21 reservoirs in the South Asian region from 2000 to 2012 was built using a multi satellite algorithm, and uncertainty analysis was conducted to improve the accuracy of estimating the water surface area for small reservoirs [30].

Except for optical satellite data, satellite radar altimetry was considered a more straightforward way to obtain water surface elevation data, based on which the actual capacity of the reservoir could be determined in one study [31]. Satellites equipped with radar and laser altimetry include Jason-1, Jason-2, ENVISAT, GFO, Topex/Poseidon and ICESat-2, with a precision of up to 5 cm, which assists in accurately assessing the water storage situation and available capacity of the reservoir [32–36]. However, small reservoirs or lakes (with small surface areas, narrow and elongated zones and complex terrain) often suffer from limited availability of elevation data derived from altimetry satellites due to issues, such as those relating to spatial resolution and satellite orbital spacing. As a result, the coverage of elevation data for these water bodies remains sparse. Therefore, elevation data derived from radar altimetry are only used for large lakes [37].

To assess the stability of reservoir storage, it is crucial to have long-term monitoring data that span a significant duration, such as a decade or more. Remote sensing data typically operate on a large scale and may have restrictions on access. However, the Google Earth Engine (GEE) serves as a valuable tool for detecting changes, visualizing historical trends and quantifying the Earth's surface. With an extensive collection of over 40 PB (petabytes) of available data, the GEE is continuously updated and expanded, offering researchers a wealth of information for analysis [38]. GFO, ERS-2 and other satellite data have been utilized to monitor the volume changes of lakes and inland seas, with the aim of establishing a global, remote sensing-based lake volume storage database [39]. Similarly, researchers have used Landsat satellite images in the GEE platform to calculate water indices for monitoring reservoir storage [40].

Extreme events, such as continuous drought, which may lead to a dramatic decrease in river discharge, result in inadequate water supply to inland lakes and reservoirs. Significant research has been carried out on drought-prone regions and inland reservoirs globally [41,42]. However, in areas where water resource scarcity is not a prevalent issue, the occurrence of historical reservoir water level decline is relatively uncommon. Furthermore, limited research and quantitative evaluation that specifically focus on estuarine reservoirs related to extreme events exist.

In this study, regarding the background of historical drought event in the river basin, we take the Qingcaosha Reservoir in the Changjiang Estuary (China) as an example and present an approach for monitoring reservoir waterlines and water levels, which serve as satellite-derived indicators of extreme drought conditions, determining if the reservoir exhibited a historical response. To achieve this main goal, we utilized CoastSat to examine remote sensing images of the estuarine reservoir. Through this approach, we monitored changes in waterline position over a time series spanning from 2013 to 2022 to assess the drought severity within the timeframe. By integrating topography data, we indirectly calculated the water level and reservoir storage corresponding to each waterline to evaluate the reservoir's responses to extreme saltwater intrusion or drought events.

2. Materials and Methods

Study Area

The study area centers around the Qingcaosha Reservoir, situated on the northwest alluvial sandbar of Changxing Island, near the river mouth of the Changjiang River in China (Figure 2). This reservoir (Figure 3A), which was constructed in the estuary, holds great economic importance for Shanghai and plays a crucial role in the well-being of its residents [43]. With a water area of about 66 km^2, a design effective capacity of 4.38×10^8 m^3 and a maximum operating water level of ~7 m [44], the Qingcaosha Reservoir has a large amount of high-quality fresh water, which meets the drinking water standard. The actual reservoir capacity is 3.8×10^8 m^3, and the water supply capacity exceeds 7.19×10^6 m^3/day, accounting for more than 50% of Shanghai's total raw water supply and benefiting more than 13 million people. Since its full operation in June 2011, the reservoir has played a vital role in Shanghai's drinking water supply, fundamentally altering the historical reliance on the Huangpu River as the primary water source [12,45]. As of early 2022, based on our information, the reservoir's water level had been consistently normal and well regulated until it was disrupted by extreme drought (Figure 1), resulting in a significant decrease in water levels (Figure 3B,C).

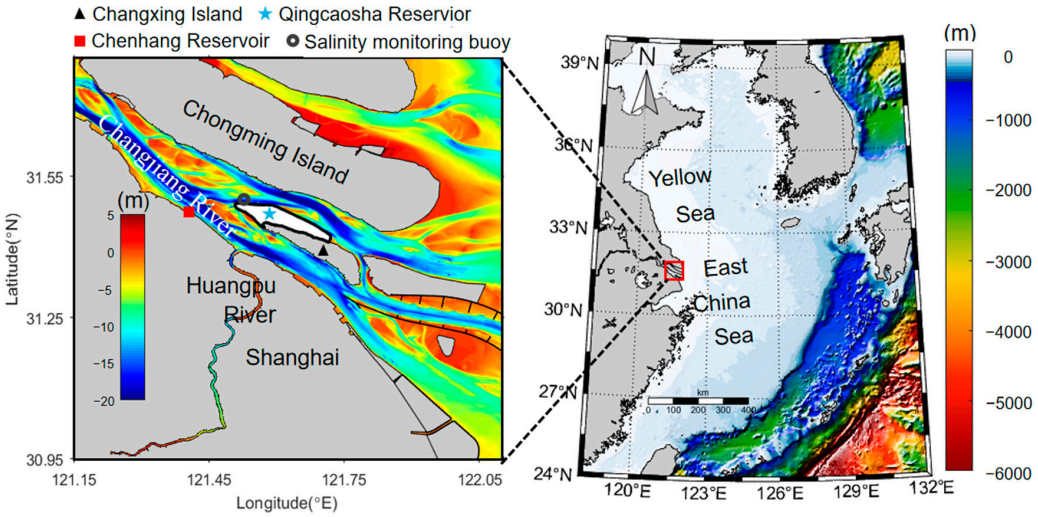

Figure 2. The location and topography of the study area. The star symbol represents the location of the Qingcaosha Reservoir, the thick solid black line represents the boundary of the reclaimed land around the reservoir, the circle indicates the position of the salinity monitoring buoy that provided the salinity data utilized in this research.

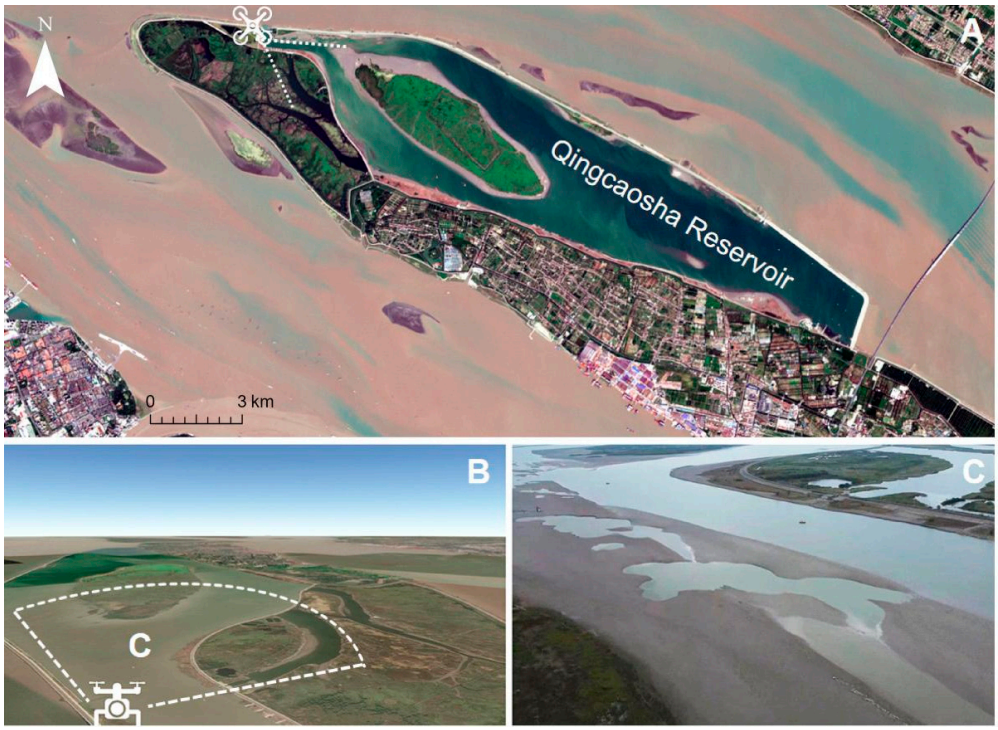

Figure 3. (**A**) Satellite imagery of the Qingcaosha Reservoir. (**B**) Satellite imagery with low-angle altitude during the period of normal water level, obtained from Google Earth. (**C**) Ariel photo taken during the low water level period, captured by an unmanned aerial vehicle (UAV) from a similar viewing perspective as (**B**).

3. Data and Methods

3.1. Satellite Imagery and Waterline Extraction

Satellite remote sensing provides cost-effective long-term image data that can address situations where in situ measurements are not available or it is inconvenient to conduct fieldwork within the desired timeframe [22].

The utilization of the CoastSat toolkit empowers users to extract waterlines from images obtained from various satellite missions, including Landsat-5, Landsat-7, Landsat-8,

Landsat-9 and Sentinel-2 satellites [46]. This tool facilitates the analysis of water bodies by enabling feature extraction from satellite optical images.

The satellite remote sensing images selected in this study are mainly from Sentinel-2 (S2) [47] and Landsat-8 (L8) [48], with data providers (USGS for Landsat or ESA for Sentinel-2), and the parameters are listed in Table 1. The former, with a revisit period of only 5 days, provided abundant image data with high spatial resolution and minimal cloud cover, enabling clear remote sensing images of the reservoir and offering advantages, such as large data volume [49]. For L8, its launch time aligns well with the operational period of the Qingcaosha Reservoir, enabling the extraction of relevant image data for a decadal analysis.

Table 1. Satellite parameters of Landsat-8 and Sentinel-2.

Satellite Name	Launch Date	Revisit Period (d)	Sensor Parameters	Spectral Range (μm)	Spatial Resolution (m)
Sentinel-2 (MSI)	23 June 2015	5	Multispectral Imager	0.4–2.4	10
Landsat-8 (OLI)	11 Feb 2013	16	Thermal Infrared Sensor	0.433–12.5	30

In the field of coastal engineering, the variation in the interface between the land and water, which is defined as the shoreline or waterline, can indicate coastal features. Many studies have used this framework to investigate coastal evolution problems [50,51]. Since there is a shallow shoal in the center of the Qingcaosha Reservoir, in this location, we employed this same approach to detect the waterline and other hydrodynamical characteristics (e.g., water level and storage). To establish a time series of satellite data for the Qingcaosha Reservoir, L8 and S2 satellite images were preprocessed from the GEE platform, covering the period from 1 January 2013 to 31 December 2022. A total of 40 images from Landsat-8 and 62 images from Sentinel-2 were obtained for the region of interest (Figure 4).

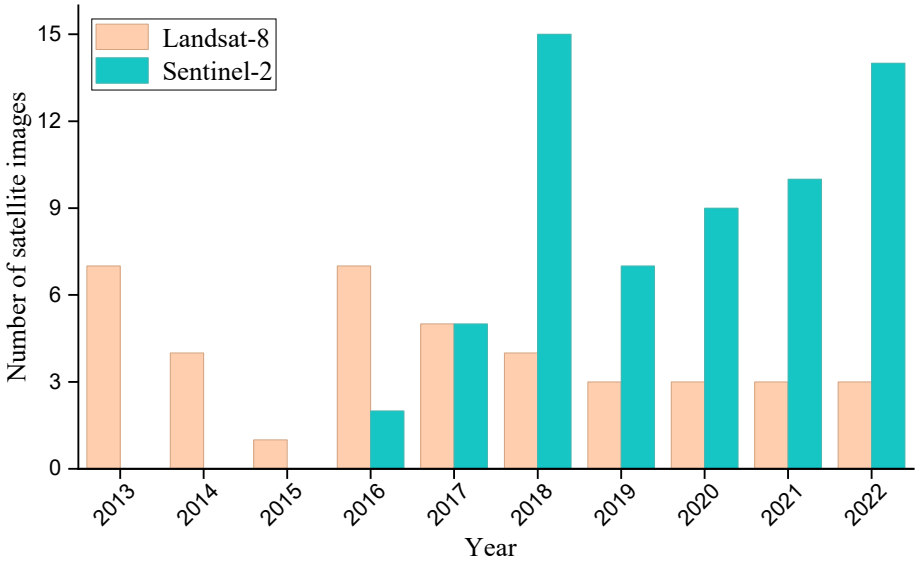

Figure 4. The number of satellite images selected for different years. The time series spans from 2013 to 2022. The S2 satellite has a larger quantity due to its shorter revisit period.

Regarding the satellite detachment methodology, an improved version of the MNDWI [52] was employed. Additionally, the waterline detection algorithm from CoastSat, which was initially designed for sandy waterlines, was adapted by adjusting relevant parameters (e.g., cloud_mask_issue, sand_color and pan_off). The modified normalized difference water index (MNDWI) equation is as follows:

$$\text{MNDWI} = \frac{\rho(G) - \rho(SWIR)}{\rho(G) + \rho(SWIR)} \quad (1)$$

where $\rho(G)$ is a band that encompasses the reflected green light and $\rho(SWIR)$ is the short-wave infrared band. The workflow diagram is illustrated in Figure 5.

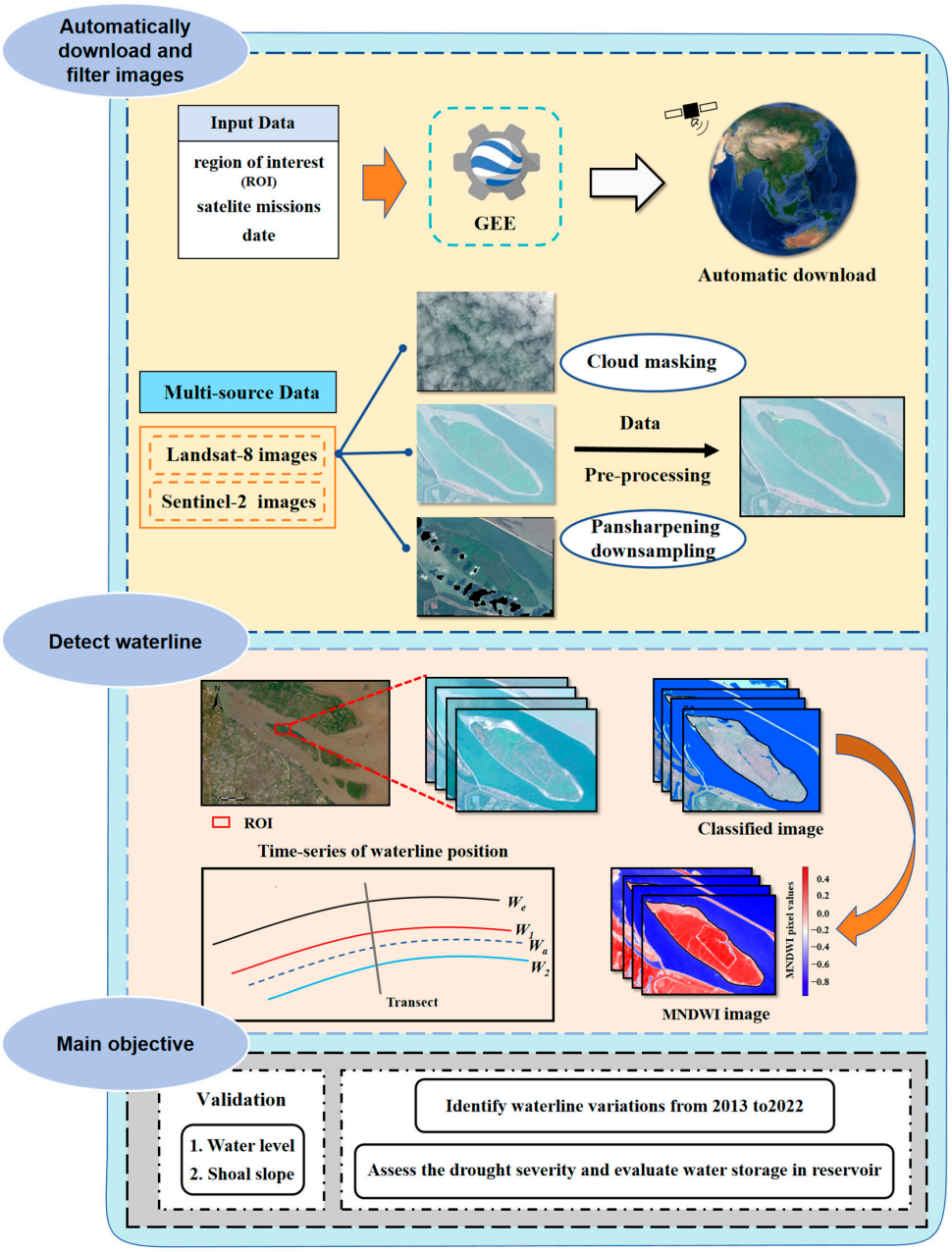

Figure 5. Flowchart of this study for downloading. **Top** panel: filtering and pre-processing satellite images; **middle** panel: detaching the waterlines from each image, ROI: region of interest, W_1 and W_2 are the normal waterline derived from satellite images, W_a and W_e represent the averaged position of normal waterlines and extreme position, respectively; (**bottom** panel).

3.2. Data Validation

The CoastSat model has been extensively calibrated, validated and applied in various studies on sandy beaches in Australia and America [53]. For muddy edges, such validation studies have also demonstrated that CoastSat can accurately reproduce waterlines, and based on several waterlines at different tidal levels, the topography of the beaches could be reconstructed [54].

In this study, we used two approaches to validate the accuracy of the extracted results.

3.2.1. Slope

We employed a single-beam echo sounder capable of real-time field measurements with centimeter-level positioning accuracy. The in situ data were collected in 2019 with a spatial resolution of 20 m. Subsequently, by assigning the monitored water levels to two waterlines (Figure 6a) during a short period (e.g., less than one month), we calculated the slope using the following equation:

$$\tan \theta_i = \frac{\Delta H}{\Delta L_i} \tag{2}$$

where θ_i represents each section slope, ΔH is the water level difference and ΔL_i is the horizontal distance between two waterlines in each section.

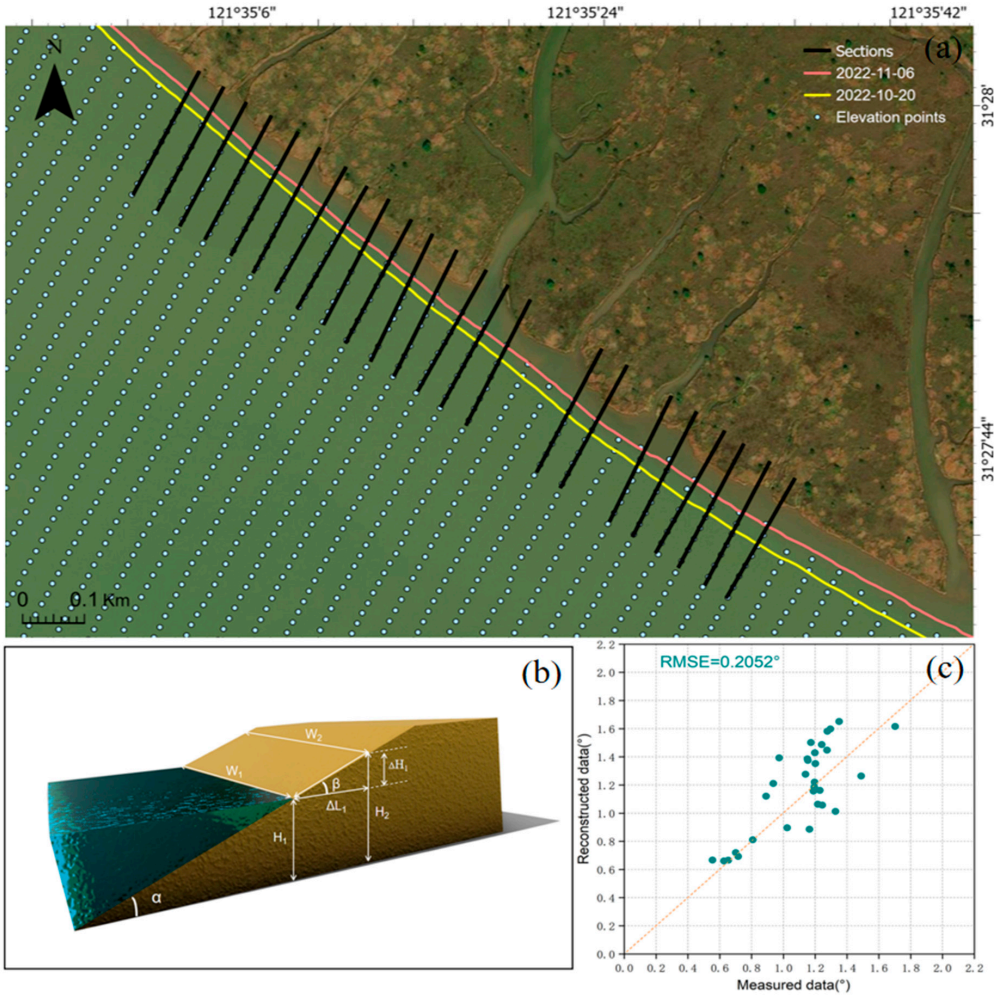

Figure 6. (**a**) The selected control section satellite image. The solid black lines indicate the control section, the red waterline corresponds to the extraction on 6 November 2022, the yellow waterline corresponds to the extraction on 20 October 2022 and the blue dot represents the topographic data points (the monitored topography was collected in 2019 with a spatial resolution of ~20 m). (**b**) A diagram of the slope on the shallow shoal in the middle of the reservoir. W_1 and W_2 represent the waterlines at different elevations, while H_1 and H_2 represent the water levels. (**c**) Comparison between the measured data obtained from different cross-sections and the reconstructed data using the water level and waterline.

$$RMSE = \sqrt{\frac{1}{n}\sum_{i=1}^{n}(X_i - Y_i)^2} \tag{3}$$

where X_i is each constructed data point, Y_i represents each measured data point and n is the number of data points.

As shown in Figure 6c, the comparison between the reconstructed slope and monitored data has an RMSE of 0.2052°.

3.2.2. Water Level

To enhance the validation of water level calculations obtained from waterlines, we adopted an alternative approach. Treat the waterlines as contour lines depicting different elevations, in accordance with the methodology outlined by [55]. The waterline captured on 2 August 2017, which was more centrally located within the given timeframe, was chosen as the reference waterline, and the corresponding water level at the same moment was assigned (2.72 m according to the monitored data). Satellite-derived water levels were calculated using Equation (4), incorporating the shoal slope and the distances between each waterline and the reference waterline. Subsequently, a comparison was conducted between these computed water levels and the concurrently recorded actual measured water level captured by the satellite during the observation of the waterline.

$$W_l = 2.72 + \Delta L \cdot \tan \alpha \tag{4}$$

where W_l is the calculated waterline level, ΔL is the distance from the reference waterline (2 August 2017) and $\tan \alpha$ is the slope of the shallow shoal.

Based on the above results, we calculated the mean absolute percentage error (*MAPE*) of the satellite inversion of the water level with the following equation:

$$MAPE = \frac{1}{n}\sum_{i=1}^{n}\left|\frac{W_i - w_i}{W_i}\right| \tag{5}$$

where W_i is water level on each measured data point, w_i represents water level on each constructed data point and n is the number of data points.

The validation of the water levels is presented in Figure 7; the water levels generated by combining topography and waterlines closely align with the in situ water levels (MAPE = 9.91%). Notably, during the winter season, it is crucial to consider the influence of saltwater intrusion, which typically necessitates higher water levels in the reservoir. The graph indicates a reduced number of estimates for high water levels, likely due to certain areas of the shoal in Qingcaosha already being submerged under high water level conditions. The estimated water levels also reflect the increasing trend on an annual scale due to the deposition of suspended sediment from the Changjiang River and the growing water demand. Because the water levels were derived based on the topography data measured in 2019, the validation performance is extensively discussed in the next subsection.

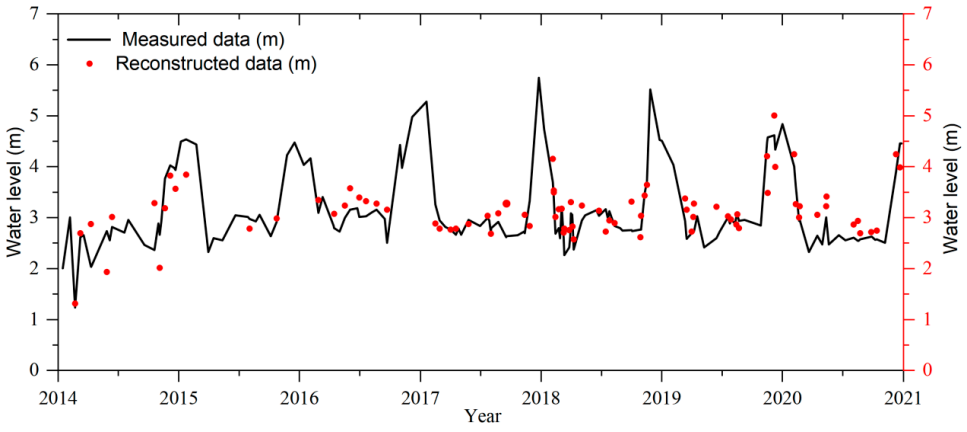

Figure 7. Time series of water level estimations (red dot) and measured data (black line) in the Qingcaosha Reservoir.

According to the above validations of slope and water level, the comparisons between the measured data and the estimated data support the reliability of the proposed method for validating slope and water level calculations. Thus, CoastSat can also be applied for extracting and analyzing waterlines in reservoirs and further evaluating the variations in reservoir storage and water resources.

3.2.3. The Reliability of Evaluating the Reservoir Water Level

To verify the reliability of the aforementioned method using optical satellite assessment, we performed error analysis across various timeframes. Since the accuracy of water level inversion and the validation of water levels between monitored data and satellite-based estimations are significantly influenced by the shoal slope or topography, we conducted validations during different timeframes from 2014 to 2020 to determine whether approaching the time (2019) when topography was measured resulted in higher accuracy (Figure 8).

Therefore, the effectiveness of verification should vary over time. Using the correlation coefficient formula to solve, the formula is obtained as follows:

$$COR(X,Y) = \frac{cov(X,Y)}{\sigma_X \sigma_Y} \tag{6}$$

$$MAE = \frac{1}{n}\sum_{i=1}^{n} \mid X_i - Y_i \mid \tag{7}$$

where X is the constructed data, Y is the measured data and n is the number of data points. cov means covariance, and σ represents the standard deviation.

Overall, the correlation coefficient for 2014 to 2020 is 0.76. Upon analyzing the comparisons year by year, the correlation coefficients range from 0.61 to 0.86, and it can be observed that the fitting performance is significantly poorer for earlier years compared to other years. This discrepancy is attributed to the utilization of terrain data from 2019, which introduces temporal differences. If there are terrain data with higher temporal and spatial resolutions, the remote sensing inversion of reservoir water level will aid in obtaining better results.

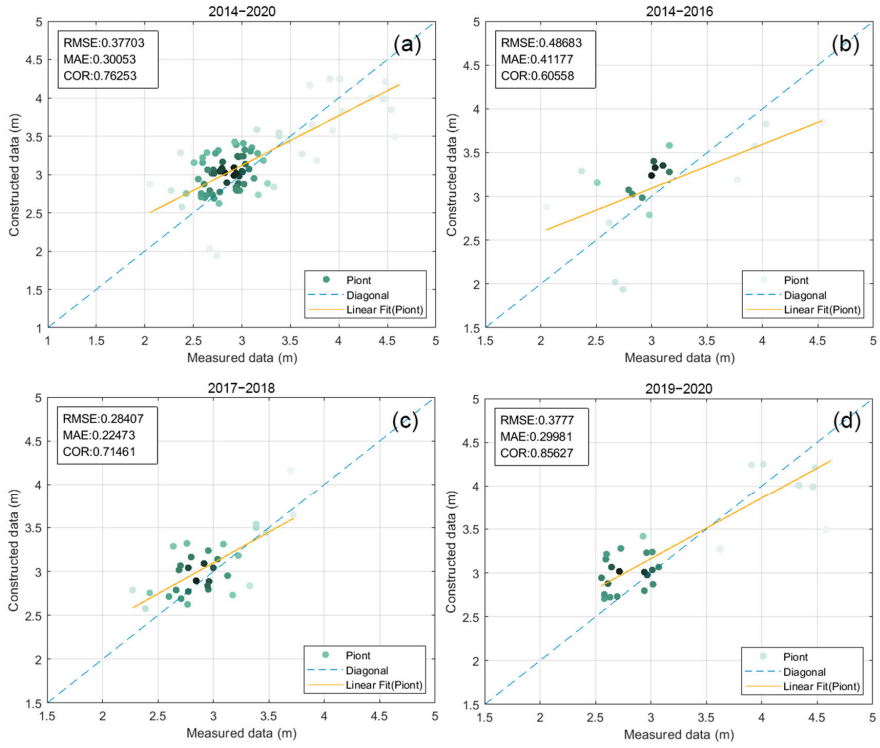

Figure 8. (**a**–**d**) Error analysis for the periods of 2014 to 2020, 2014 to 2016, 2017 to 2018 and 2019 to 2020. The graph displays the results of RMSE, MAE and COR.

4. Results

4.1. Extraction of the Waterlines around the Shallow Shoal in the Qingcaosha Reservoir

Registering and correcting satellite images from different periods enables the positional information of waterlines to be acquired at different times, thus providing information about water level changes. The waterline ensemble maps extracted from satellite images reveal that the area of the shoal in the Qingcaosha Reservoir stands out significantly from the normal water level on 21 February 2014 and 15 October 2022, with the latter showing a more pronounced expansion of the waterline than the former (Figures 9 and 10).

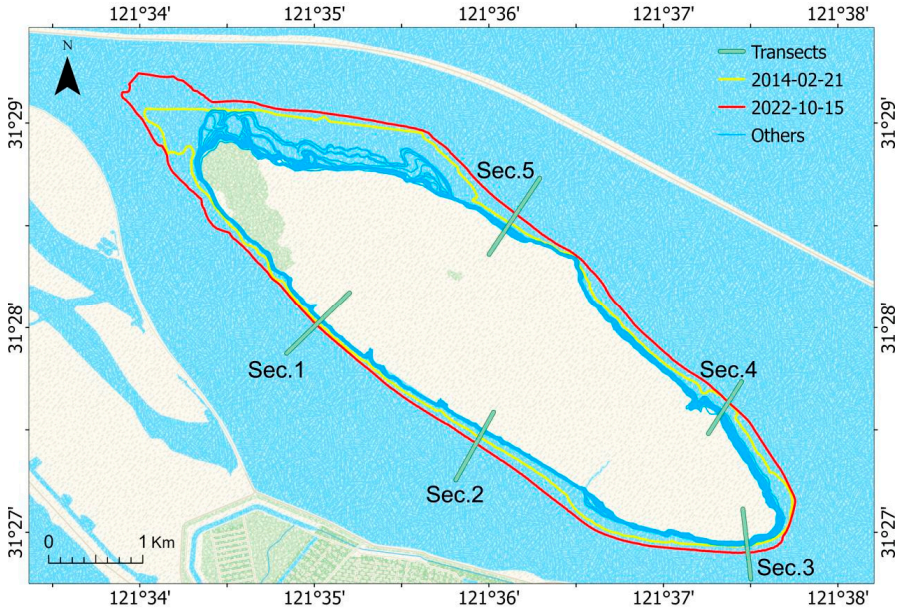

Figure 9. Compilation of waterlines around the shoal in the Qingcaosha Reservoir. All waterlines were extracted from satellite imagery using CoastSat. The red line represents the waterline on 15 October 2022, and the yellow line corresponds to the waterline on 21 February 2014. The blue lines represent the waterline extracted from other years. Sections 1 to 5 are the selected cross-sections of the waterlines.

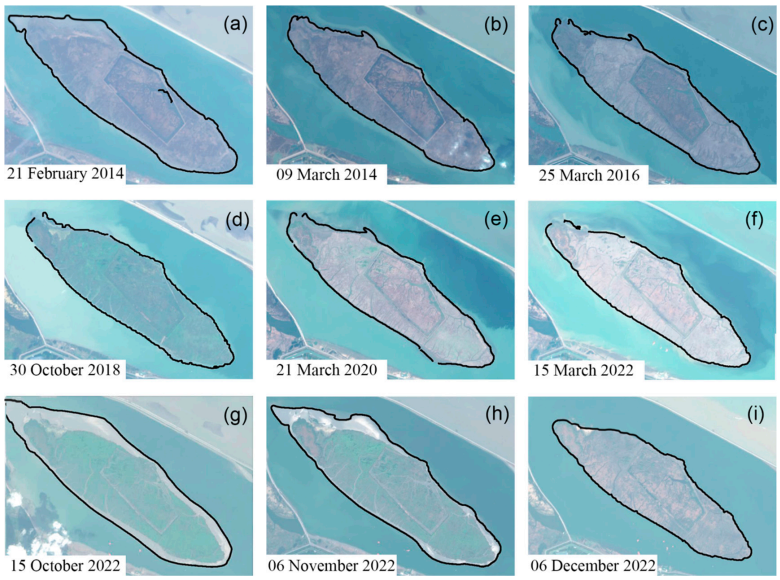

Figure 10. Multitemporal remote sensing images from different satellite sources and selected outputs from CoastSat Images. (**a**–**i**) represent the original satellite images, where (**a**–**c**) are from Landsat-8 and (**d**–**i**) are from Sentinel-2. The solid black line represents the waterline calculated by CoastSat.

Based on the satellite images captured in December 2022, the water level in the reservoir returned to its normal level as in previous years. Notably, the accuracy of the CoastSat mapping technique in the shallow areas in the shoal in the reservoir is remarkably high, particularly in the area enclosed by waterline points (a) and (g). This significant area indicates the current critical water level, emphasizing the need for attention from water management authorities.

4.2. Assessment of the Reservoir Drought Severity

To quantify the reservoir drought severity over the past decade and evaluate the resilience of the reservoir, the variations in the distance between each waterline and the reference waterline along five sections are shown in Figure 11. The variations in salinity response at the reservoir intake to river mouth droughts are illustrated in Figure 12. The salinity threshold for reservoir water intake is 0.45. If the salinity exceeds 0.45 for a prolonged period, it will disrupt the water level balance.

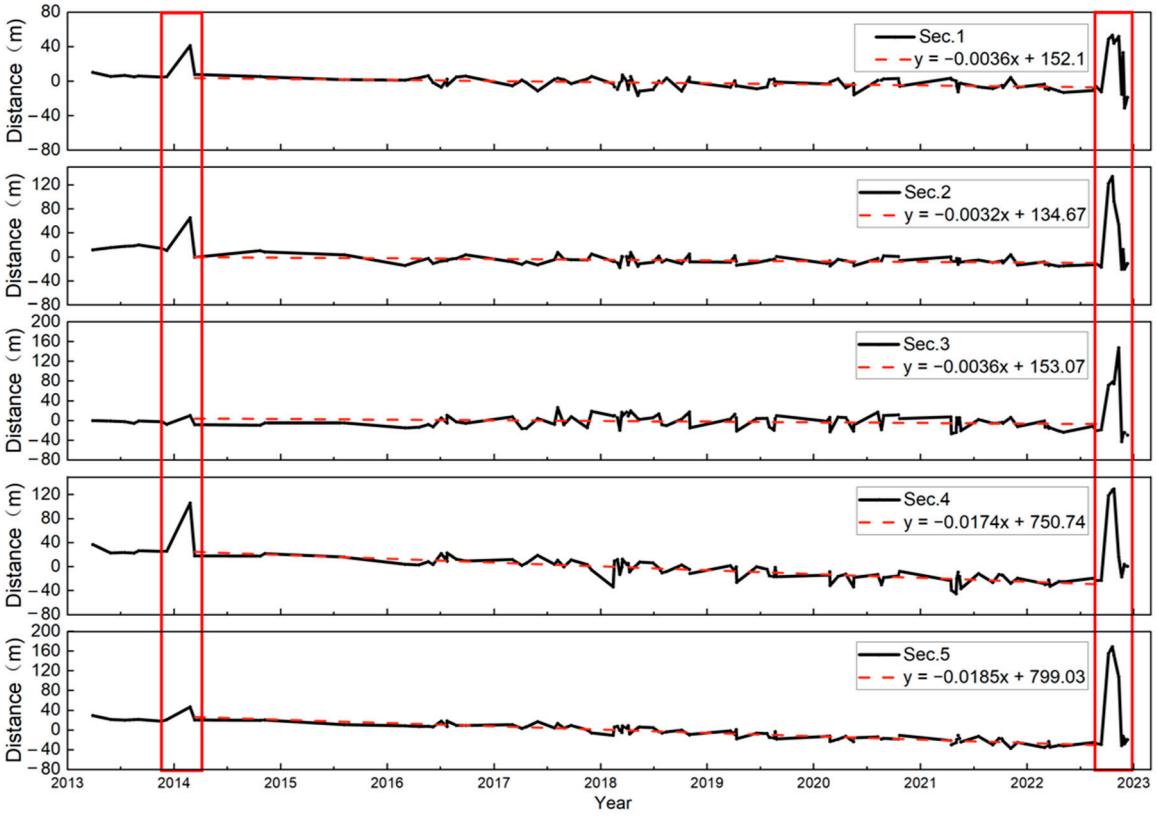

Figure 11. Time series trends of waterline spanning from 2013 to 2022. Sections 1 to 5 represent the selected cross-sections of the waterlines (locations are shown in Figure 9). Positive values correspond to lower water levels. The red boxes mark two significant instabilities in the past decade. The dashed lines are the trendlines within this timeframe.

In February 2014, the Qingcaosha Reservoir was experiencing a water shortage emergency caused by strong saltwater intrusion, which was driven by the long-persistent, strong northerly wind [11], resulting in a 23-day interruption in freshwater intake (Figure 12a). Comparing the peak heights highlighted in the red boxes, the waterline in 2022 is much farther than the event in 2014 (Figure 11), resulting in a 98-day interruption of the freshwater intake from September to December (Figure 12b). Performing linear regression on the data between the two peaks indicates that the water level in the Qingcaosha Reservoir is in a state of gradually increasing, which coincides with the trend of monitored water levels (Figure 11). This extremely low water level in the reservoir was caused by the most severe saltwater intrusion in 2022 due to prolonged very low river discharge. The water level,

calculated from the extracted waterline on 15 October 2022, was estimated to be 0.722 m. In contrast to the well-regulated storage level (approximately 2.5–5.5 m, as shown in Figure 7), the water level plummeted to its historically lowest value, even lower than that recorded in February 2014 (1.32 m, as depicted in Figure 7). After 15 October, the reservoir water level gradually began to recover, leading to an increasing trend in the reservoir's water surface area.

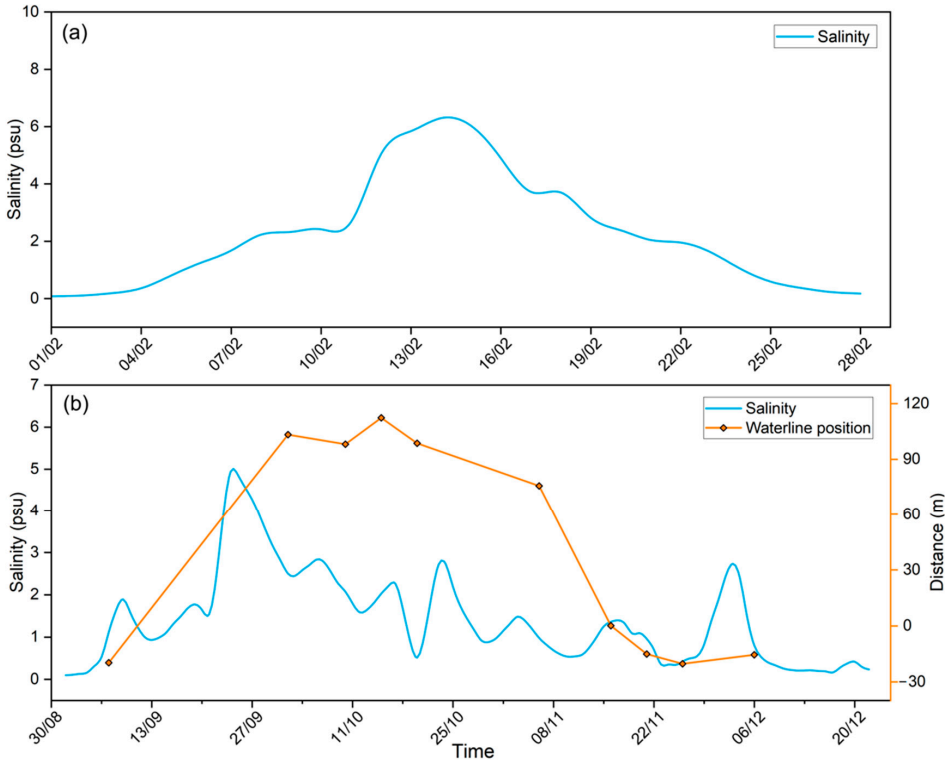

Figure 12. (**a**) The salinity variation at the water intake of the Qingcaosha Reservoir in February 2014. (**b**) The blue line represents the salinity variation from September to December in 2022, and the red line represents the relative position of each waterline.

4.3. Storage Capacity Evaluation of the Qingcaosha Reservoir

When assessing regional drought, the reservoir storage capacity is an important indicator in addition to the water level of the reservoir. However, due to the lack of reservoir storage capacity information or issues regarding data transparency, it is difficult to obtain comprehensive and accurate information on reservoir storage capacity, which affects the accuracy of drought assessment and monitoring and hampers the formulation and implementation of drought response measures [56]. Therefore, obtaining and updating reservoir capacity information is crucial for drought management and decision making. In this study, a method based on CoastSat-extracted waterline data (Figure 9) is proposed to estimate the reservoir storage capacity using topography data and water level data in the Qingcaosha Reservoir. The water area is calculated using threshold segmentation applied to the extracted waterline data, while the water depth is calculated using topography and water level data. The topography data are obtained in 2019, after which the storage reservoir capacity can be calculated from them, as shown in the formula:

$$V(H) = \sum_{i=1}^{n} (H - h_i) \cdot A_i \tag{8}$$

where V denotes water storage at water level H; h_i denotes the pixel value of the topography (in m); n is the number of pixels of the topography inside the mask, and A_i represents the area of each orthogonal grid. The extent of the calculation is determined by the waterline data and the reservoir boundary.

By interpolating the monitored depth to orthogonal grids with fixed areas and corresponding to the water levels through the locations of the waterline, the total volume variations in the Qingcaosha Reservoir were calculated. When the reservoir water level is at the dead water level, the corresponding reservoir storage is approximately 1.01×10^8 m^3 (Figure 13c), which is close to the reported value [44]. Therefore, we use this method to calculate the reservoir storage capacity under the following conditions: when the water level is operating normally, the calculated reservoir storage capacity is 3.92×10^8 m^3 (Figure 13d). In extreme events, the lowest storage capacities in 2014 and 2022 were 1.82×10^8 and 1.65×10^8 m^3, respectively. Under the influence of extreme events, the storage capacity obviously decreased, but the corresponding storage at the lowest water level of the reservoir was still higher than the dead storage, indicating the reservoir's robust resilience during the historical extreme drought event.

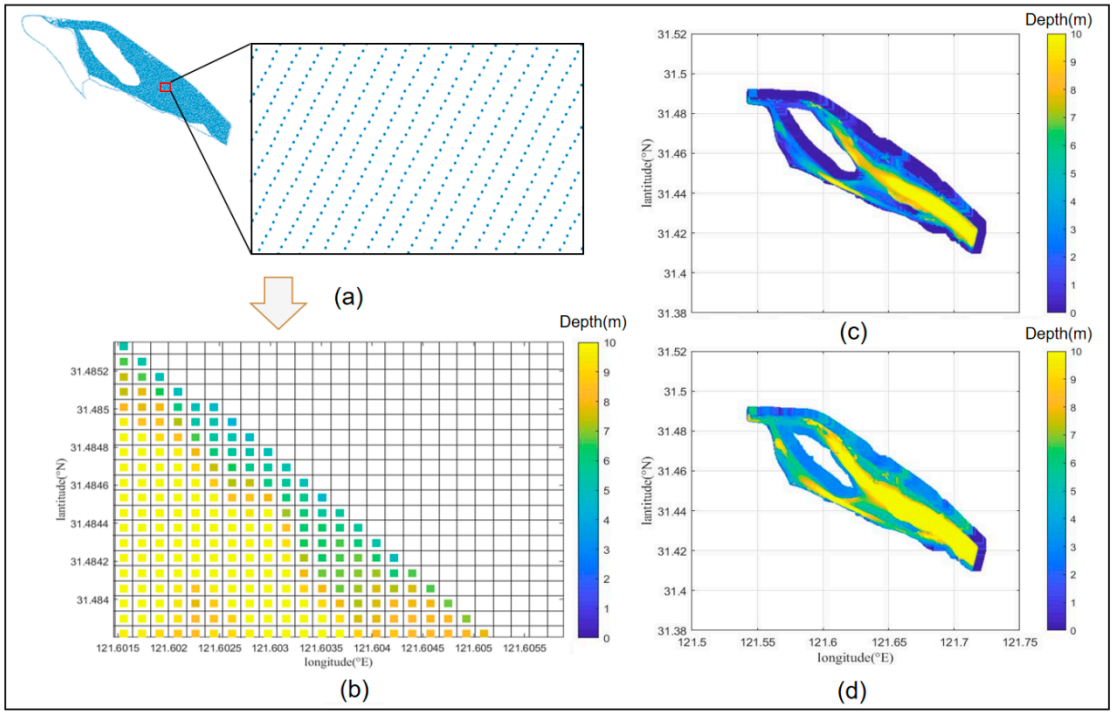

Figure 13. (**a**) The blue dots represent topographic data points. (**b**) The reservoir volume computation model, which utilizes the waterline and interpolates topographic data to determine the reservoir's water depth. Each grid cell contains a water depth value, with different colors representing varying depths. (**c**,**d**) depict the minimum storage and maximum storage, respectively.

5. Discussion

The Qingcaosha Reservoir, which provides water to 13 million people in Shanghai, experienced a severe drought and saltwater intrusion in the autumn and winter of 2022. This drought was the worst in the Changjiang River Basin in 61 years, which reduced the upstream water inflow and allowed seawater to flow into the river and salinize the water. The reservoir had to close its water intake from 5 September to 12 December, a total of 97 days, to prevent saltwater contamination. This occurrence significantly affected Shanghai's water supply and security. The reservoir can store fresh water for 68 days when it is full [43], but it is vulnerable to saltwater intrusion under very low river discharge. Saltwater intrusion usually occurs from October to March of the following year [57], but it started earlier in 2022 due to the continuous drought in summer and autumn and resulted in a total of 97 days of unsuitable water intake.

With the intensification of global climate change, the occurrence of extreme drought events is becoming frequent. The 2022 extreme drought event had a significant impact on reservoir storage around the world. In the U.S., the drought caused some major reservoirs such as Lake Mead and Lake Powell to drop to their lowest levels on record, threatening the water supply and hydropower generation for millions of people. Statewide reservoir storage was 69 percent of average for this time of year [58]. In Europe, at the end of summer 2022, the drought emergency seemed partially overcome. However, as of October 2022, the water storage levels in some reservoirs remain significantly below the reference values for this timeframe. This situation is likely to heighten awareness of the risks associated with extreme droughts on freshwater supply in Europe [59]. In China, the drought also lowered the water level of Poyang Lake, the largest freshwater lake in China, to its lowest level since 1955. The minimum area of Poyang Lake estimated by satellite data was 814 km^2, which matched well with the observed drought characteristics [60]. In the recent research focused on drought assessment within the Changjiang River Basin, satellites equipped with altimeters were used [61,62]. However, this approach may not be appropriate for the Qingcaosha Reservoir due to its smaller spatial scale. Consequently, employing a method that extracts the waterline to assess drought severity would be more suitable.

We also employed the aforementioned method to monitor reservoirs situated in the Pearl River Estuary, such as the Zhuyin Reservoir, as well as other estuary reservoirs in South Korea, including the Ganwol Estuary Reservoir and Youngsan Estuary Reservoir. Additionally, remote sensing monitoring has also been employed to monitor several inland reservoirs for comparison.

The results showed that the water levels of the inland reservoirs decreased significantly during the dry hydrological year of 2022 (Figure 14a–e). However, most of the estuarine reservoirs in water-rich areas did not exhibit such noticeable changes in water levels, except for the Zhuyin Reservoir (Figure 14h).

Nevertheless, this method also has the following limitations: it is applicable to reservoirs with relatively small surface slope gradients, and in such cases, the variations near the waterline are more pronounced, making it possible to further analyze the migration of data identified by CoastSat. For example, the Chenhang Reservoir (Figure 14i), located in the Changjiang River Estuary, also had closed water intake points, but due to the steep slopes surrounding the reservoir, no significant changes were observed within the known waterlines using CoastSat.

Additionally, the temporal resolution for selecting remote sensing data in the toolkit is limited. Although satellite remote sensing data can provide extensive coverage, their temporal resolution may be constrained, meaning that they may not capture all short-term water level changes. The accuracy of remote sensing data is also limited. While satellite remote sensing data can capture changes in reservoir water levels, their accuracy is influenced by various factors, which can lead to errors in the remote sensing data and inaccurate detection of water level changes.

The results of our research can provide information for water resource management decisions and promote the sustainable development of estuarine reservoirs as important water sources. Further research is needed to comprehensively investigate the potential of other remote sensing techniques in monitoring water resources and managing water resource utilization.

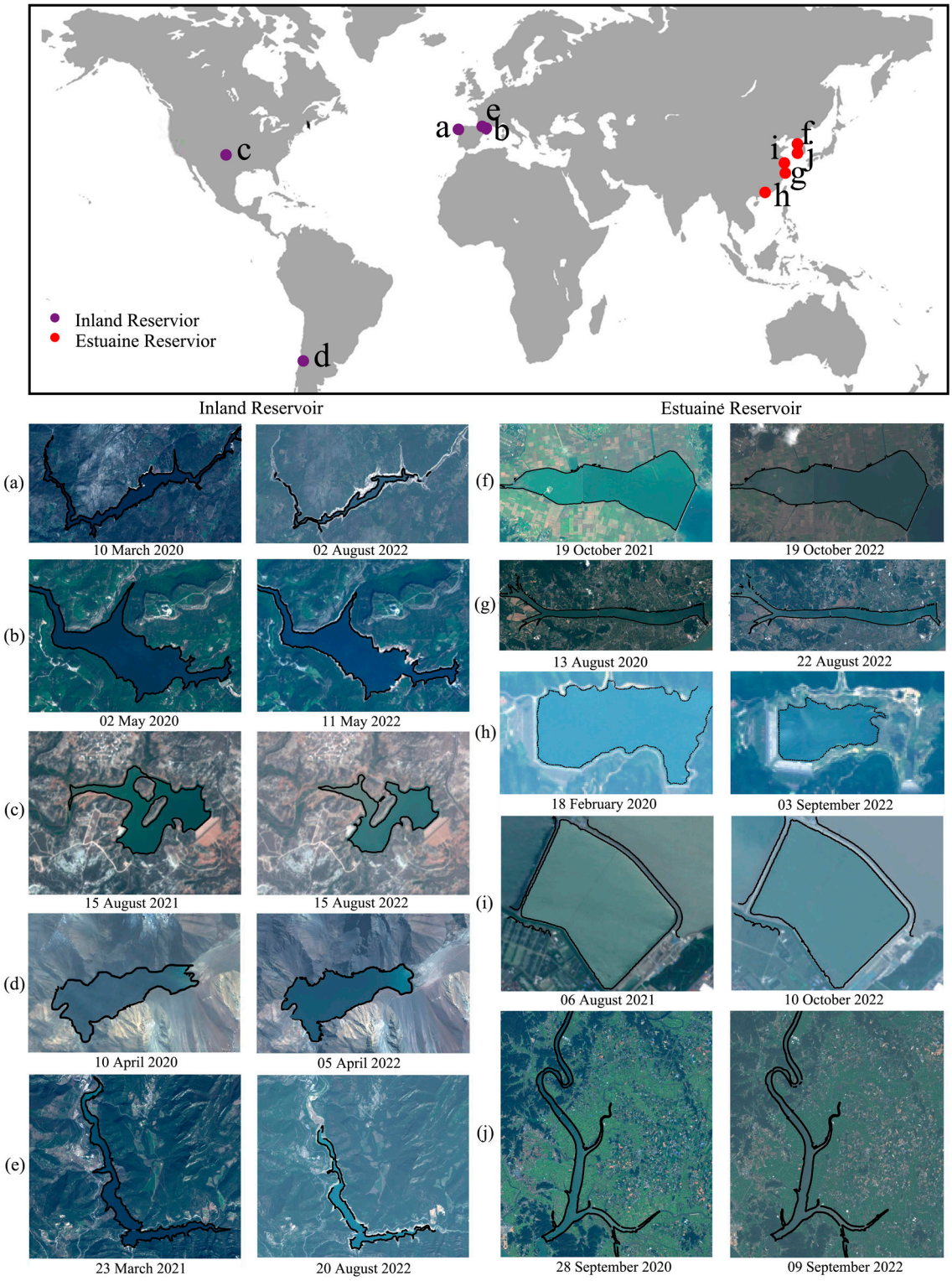

Figure 14. Locations of the studied reservoirs. (**a**–**j**) Waterside map of reservoirs at different times extracted by CoastSat. (**a**–**e**) Inland reservoirs, including the Alto Lindoso reservoir, Sau reservoir, Mackenzie reservoir, EI Yeso reservior and Baells reservoir. (**f**–**j**) Estuary reservoirs, including the Ganwol Estuary reservoir, Huchengang reservoir, Zhuyin reservoir, Chenhang reservoir and Yeongsan reservoir.

6. Conclusions

In 2022, the Changjiang River reached record low levels in August. Consequently, the reservoirs along the Changjiang River encountered drought conditions, including the estuarine reservoir, which was previously believed to have sufficient water during the summer. Remote sensing inversion stands out as a crucial method for investigating issues related to reservoir drought. Although, the method that employs optical satellite imagery to derive water levels is dependent on topographical data, specifically high spatial resolution data and gentle slopes near the waterline, in contrast to techniques that utilize satellites equipped with altimeters. It may be better suited for studies of reservoirs on a small scale (on the order of several kilometers). Therefore, we used the satellite-derived waterline position as an indicator to identify the drought severity in the remote sensing records of the Qingcaosha Reservoir.

Based on the GEE platform, utilizing 102 images from Landsat-8 and Sentinel-2 satellites, the time series of the Qingcaosha Reservoir from 2013 to 2022 can be rapidly and accurately processed to monitor the water area extent and shallow shoal area changes dynamically. CoastSat, which was previously used for coastline extraction, was successfully employed for the first time to extract the waterlines of estuarine reservoirs in this paper. By training the algorithm with appropriate datasets and adjusting relevant parameters, satisfactory results are achieved in mapping the waterlines of the Qingcaosha Reservoir. Utilizing this algorithm, the lowest water level since the reservoir's establishment was indirectly captured by using the waterlines as an indication, which reached 0.722 m in October 2022 and was significantly lower than the well-regulated water level (~2.5–5.5 m). The second lowest water level, 1.32 m, was observed in the satellite image from February 2014. The two severe drought events were induced by notable saltwater intrusions in the Changjiang River Estuary. The most severe event was triggered by an overall drought affecting the entire river basin throughout the flood season of 2022, while the other resulted from the prolonged and robust northerly winds during the dry season of 2014. The low water level phenomenon persisted for approximately 3 months, spanning August to November 2022. Despite returning to the normal level following an increase in river discharge, the occurrence of two severe drought events in the reservoir not only deserves attention but also serves as a notable example of how estuarine reservoirs respond to saltwater intrusion during both flood and dry seasons. Furthermore, the lowest actual reservoir storage levels in 2014 and 2022 were evaluated at 1.82×10^8 and 1.65×10^8 m^3, which are still higher than that for dead storage (1.01×10^8 m^3), highlighting the reservoir's significant resilience. The discussion of the remote sensing technique utilized in this study reveals that its effectiveness and precision in determining water levels are contingent upon the topographical characteristics of the reservoir. This highlights a constraint in applying this method to reservoirs that either lack detailed topographical data or feature steep slopes, underscoring the method's limitations in such environments.

The Qingcaosha Reservoir has maintained a stable balance between water supply and demand for a decade. Extreme drought events upset this balance and cause water level fluctuations and water shortages. Similar events in reservoirs located in wet regions around the globe rarely exhibit such phenomena, indicating the rarity of this occurrence.

In the context of extreme drought, it is observed that even water supply reservoirs located in nonwater-stressed regions experienced critical water levels. In the future, further attention will be given to satellite data for more detailed and in-depth research and analysis of resilience to estuarine reservoirs worldwide, which will enable long-term monitoring of extreme drought events and their impacts.

Author Contributions: Conceptualization R.Y. and C.Q.; investigation R.Y. and C.Q.; data curation J.Z. and C.Q.; methodology R.Y. and R.X.; validation R.X. and H.Z.; writing—original draft preparation R.Y. and R.X.; writing—review and editing J.Z. All authors have read and agreed to the published version of the manuscript.

Funding: This research was funded by the National Natural Science Foundation of China (42306190, 42276174) and Shanghai Municipal Oceanic Bureau (hhk202004), Shanghai Frontiers Science Center of 'Full Penetration' Far-Reaching Offshore Ocean Energy and Power (founded by the Shanghai Municipal Commission of Education).

Data Availability Statement: Data used in this paper can be provided by Rui Yuan (yuanrui@shmtu.edu.cn) upon request. The data are not publicly available due to the confidentiality of the data.

Acknowledgments: Several open-source toolboxes were used in this study, including CoastSat (see reference) and M_map (https://www.eoas.ubc.ca/~rich/map.html, accessed on 20 December 2022).

Conflicts of Interest: The authors declare no conflicts of interest.

References

1. Leuven, J.R.; Pierik, H.J.; Vegt, M.V.D.; Bouma, T.J.; Kleinhans, M.G. Sea-level-rise-induced threats depend on the size of tide-influenced estuaries worldwide. *Nat. Clim. Chang.* **2019**, *9*, 986–992. [CrossRef]
2. Zhu, J.; Wu, H.; Li, L.; Qiu, C. *Saltwater intrusion in the Changjiang Estuary. Coastal Environment, Disaster, and Infrastructure-A Case Study of China's Coastline*; IntechOpen: Rijeka, Croatia, 2018; pp. 49–73.
3. Harrison, L.M.; Coulthard, T.J.; Robins, P.E.; Lewis, M.J. Sensitivity of estuaries to compound flooding. *Estuar. Coasts* **2022**, *45*, 1250–1269. [CrossRef]
4. Olisah, C.; Adams, J.B. Analysing 70 years of research output on South African estuaries using bibliometric indicators. *Estuar. Coast. Shelf Sci.* **2021**, *252*, 107285. [CrossRef]
5. McLusky, D.S.; Elliott, M. *The Estuarine Ecosystem: Ecology, Threats, and Management*, 3rd ed.; Oxford University Press: Oxford, UK; New York, NY, USA, 2004; ISBN 978-0-19-853091-6.
6. Jeong, Y.H.; Yang, J.S.; Park, K. Changes in Water Quality After the Construction of an Estuary Dam in the Geum River Estuary Dam System, Korea. *J. Coast. Res.* **2014**, *298*, 1278–1286. [CrossRef]
7. Te, S.H.; Gin, K.Y.-H. The dynamics of cyanobacteria and microcystin production in a tropical reservoir of Singapore. *Harmful Algae* **2011**, *10*, 319–329. [CrossRef]
8. Mishra, A.K.; Singh, V.P. A review of drought concepts. *J. Hydrol.* **2010**, *391*, 202–216. [CrossRef]
9. Shah, D.; Zhao, G.; Li, Y.; Singh, V.P.; Gao, H. Assessing Global Reservoir-Based Hydrological Droughts by Fusing Storage and Evaporation. *Geophys. Res. Lett.* **2024**, *51*, e2023GL106159. [CrossRef]
10. Gibson, R.N.; Barnes, M.; Atkinson, R.J.A. Impact of changes in flow of freshwater on estuarine and open coastal habitats and the associated organisms. *Oceanogr. Mar. Biol. Annu. Rev.* **2002**, *40*, 233.
11. Oliveira, V.H.; Sousa, M.C.; Morgado, F.; Dias, J.M. Modeling the Impact of Extreme River Discharge on the Nutrient Dynamics and Dissolved Oxygen in Two Adjacent Estuaries (Portugal). *JMSE* **2019**, *7*, 412. [CrossRef]
12. Zhu, J.; Cheng, X.; Li, L.; Wu, H.; Gu, J.; Lyu, H. Dynamic Mechanism of an Extremely Severe Saltwater Intrusion in the Changjiang Estuary in February 2014. *Hydrol. Earth Syst. Sci.* **2020**, *24*, 5043–5056. [CrossRef]
13. Bellafiore, D.; Ferrarin, C.; Maicu, F.; Manfè, G.; Lorenzetti, G.; Umgiesser, G.; Zaggia, L.; Levinson, A.V. Saltwater Intrusion in a Mediterranean Delta Under a Changing Climate. *J. Geophys. Res. Oceans* **2021**, *126*, e2020JC016437. [CrossRef]
14. Brunner, M.I.; Slater, L.; Tallaksen, L.M.; Clark, M. Challenges in modeling and predicting floods and droughts: A review. *Wiley Interdiscip. Rev.* **2021**, *8*, e1520. [CrossRef]
15. Liu, X.; Hou, K.; Jia, H.; Zhao, J.; Mili, L.; Jin, X.; Wang, D. A Planning-Oriented Resilience Assessment Framework for Transmission Systems Under Typhoon Disasters. *IEEE Trans. Smart Grid* **2020**, *11*, 5431–5441. [CrossRef]
16. Li, L.; Wang, C.; Pareja-Roman, L.F.; Zhu, J.; Chant, R.J.; Wang, G. Effects of Typhoon on Saltwater Intrusion in a High Discharge Estuary. *J. Geophys. Res. Oceans* **2022**, *127*, e2021JC018206. [CrossRef]
17. Chow, D. 2022 Was the Year of Drought. Available online: https://www.nbcnews.com/science/environment/2022-was-year-drought-rcna62410 (accessed on 31 December 2023).
18. Mikhailov, V.N.; Korotaev, V.N.; Mikhailova, M.V.; Congxian, L.; Shuguang, L. Hydrological Regime and Morphodynamics of the Changjiang River Mouth Area. *Water Resour.* **2001**, *28*, 351–363. [CrossRef]
19. Sigurdsson, J.; Armannsson, S.E.; Ulfarsson, M.O.; Sveinsson, J.R. Fusing Sentinel-2 and Landsat 8 Satellite Images Using a Model-Based Method. *Remote Sens.* **2022**, *14*, 3224. [CrossRef]
20. Qiu, C.; Zhu, J.-R. Influence of Seasonal Runoff Regulation by the Three Gorges Reservoir on Saltwater Intrusion in the Changjiang River Estuary. *Cont. Shelf Res.* **2013**, *71*, 16–26. [CrossRef]
21. Duan, Z.; Bastiaanssen, W.G.M. Estimating Water Volume Variations in Lakes and Reservoirs from Four Operational Satellite Altimetry Databases and Satellite Imagery Data. *Remote Sens. Environ.* **2013**, *134*, 403–416. [CrossRef]
22. Sheffield, J.; Wood, E.F.; Pan, M.; Beck, H.; Coccia, G.; Serrat-Capdevila, A.; Verbist, K. Satellite Remote Sensing for Water Resources Management: Potential for Supporting Sustainable Development in Data-Poor Regions. *Water Resour. Res.* **2018**, *54*, 9724–9758. [CrossRef]

23. Zhao, J.; Zhang, F.; Chen, S.; Wang, C.; Chen, J.; Zhou, H.; Xue, Y. Remote Sensing Evaluation of Total Suspended Solids Dynamic with Markov Model: A Case Study of Inland Reservoir across Administrative Boundary in South China. *Sensors* **2020**, *20*, 6911. [CrossRef]
24. Wu, Q.; Ke, L.; Wang, J.; Pavelsky, T.M.; Allen, G.H.; Sheng, Y.; Duan, X.; Zhu, Y.; Wu, J.; Wang, L.; et al. Satellites Reveal Hotspots of Global River Extent Change. *Nat. Commun.* **2023**, *14*, 1587. [CrossRef]
25. Yao, F.; Livneh, B.; Rajagopalan, B.; Wang, J.; Crétaux, J.-F.; Wada, Y.; Berge-Nguyen, M. Satellites Reveal Widespread Decline in Global Lake Water Storage. *Science* **2023**, *380*, 743–749. [CrossRef]
26. Li, X.; Tao, R.; Zhang, K. Drought Monitoring Based on Remote Sensing. In *Remote Sensing of Water-Related Hazards*; Wiley: Hoboken, NJ, USA, 2022; pp. 149–168.
27. Yang, X.; Zhao, S.; Qin, X.; Zhao, N.; Liang, L. Mapping of Urban Surface Water Bodies from Sentinel-2 MSI Imagery at 10 m Resolution via NDWI-Based Image Sharpening. *Remote Sens.* **2017**, *9*, 596. [CrossRef]
28. Ali, M.I.; Dirawan, G.D.; Hasim, A.H.; Abidin, M.R. Detection of Changes in Surface Water Bodies Urban Area with NDWI and MNDWI Methods. International Journal on Advanced Science. *Eng. Inf. Technol.* **2019**, *9*, 946.
29. Gao, H.; Birkett, C.; Lettenmaier, D.P. Global Monitoring of Large Reservoir Storage from Satellite Remote Sensing. *Water Resour. Res.* **2012**, *48*, 2012WR012063. [CrossRef]
30. Zhang, S.; Gao, H.; Naz, B.S. Monitoring reservoir storage in South Asia from multisatellite remote sensing. *Water Resour. Res.* **2014**, *50*, 8927–8943. [CrossRef]
31. Calmant, S.; Seyler, F.; Cretaux, J.F. Monitoring Continental Surface Waters by Satellite Altimetry. *Surv. Geophys.* **2008**, *29*, 247–269. [CrossRef]
32. Birkett, C.M.; Beckley, B. Investigating the Performance of the Jason-2/OSTM Radar Altimeter over Lakes and Reservoirs. *Mar. Geod.* **2010**, *33*, 204–238. [CrossRef]
33. Frappart, F.; Seyler, F.; Martinez, J.-M.; León, J.G.; Cazenave, A. Floodplain Water Storage in the Negro River Basin Estimated from Microwave Remote Sensing of Inundation Area and Water Levels. *Remote Sens. Environ.* **2005**, *99*, 387–399. [CrossRef]
34. Ričko, M.; Birkett, C.M.; Carton, J.A.; Crétaux, J.-F. Intercomparison and Validation of Continental Water Level Products Derived from Satellite Radar Altimetry. *J. Appl. Remote Sens.* **2012**, *6*, 061710. [CrossRef]
35. Zou, Y.; Greenberg, J.A. A Spatialized Classification Approach for Land Cover Mapping Using Hyperspatial Imagery. *Remote Sens. Environ.* **2019**, *232*, 111248. [CrossRef]
36. Wang, Y.; Long, D.; Li, X. High-temporal-resolution monitoring of reservoir water storage of the Lancang-Mekong River. *Remote Sens. Environ.* **2023**, *292*, 113575. [CrossRef]
37. Maswanganye, S.E.; Dube, T.; Mazvimavi, D.; Jovanovic, N. Remotely Sensed Applications in Monitoring the Spatio-Temporal Dynamics of Pools and Flows along Non-Perennial Rivers: A Review. *South Afr. Geogr. J.* **2022**, *104*, 427–445. [CrossRef]
38. Gorelick, N.; Hancher, M.; Dixon, M.; Ilyushchenko, S.; Thau, D.; Moore, R. Google Earth Engine: Planetary-Scale Geospatial Analysis for Everyone. *Remote Sens. Environ.* **2017**, *202*, 18–27. [CrossRef]
39. Li, H.; Luo, Z.; Xu, Y.; Zhu, S.; Chen, X.; Geng, X.; Xiao, L.; Wan, W.; Cui, Y. A remote sensing-based area dataset for approximately 40 years that reveals the hydrological asynchrony of Lake Chad based on Google Earth Engine. *J. Hydrol.* **2021**, *603*, 126934. [CrossRef]
40. Condeça, J.; Nascimento, J.; Barreiras, N. Monitoring the Storage Volume of Water Reservoirs Using Google Earth Engine. *Water Resour. Res.* **2022**, *58*, e2021WR030026. [CrossRef]
41. Zhao, G.; Gao, H. Towards Global Hydrological Drought Monitoring Using Remotely Sensed Reservoir Surface Area. *Geophys. Res. Lett.* **2019**, *46*, 13027–13035. [CrossRef]
42. Xu, N.; Ma, Y.; Wei, Z.; Huang, C.; Li, G.; Zheng, H.; Wang, X.H. Satellite Observed Recent Rising Water Levels of Global Lakes and Reservoirs. *Environ. Res. Lett.* **2022**, *17*, 074013. [CrossRef]
43. Zhu, J.R.; Gu, Y.L.; Wu, H. Determination of the period not suitable for taking domestic water supply to the Qingcaosha Reservoir near Changjiang River Estuary. *Oceanol. Limnol. Sin.* **2013**, *44*, 1138–1145.
44. Yuan, J.Z.; Wu, C.E. Shanghai Coastal Reservoirs: Their Development and Experience from Their Design. *HydrolinkIahrCoast. Res.* **2018**, 10–13. Available online: https://iahr.oss-accelerate.aliyuncs.com/library/HydroLink/HydroLink2018_01_Coastal_Reservoirs.pdf (accessed on 10 June 2023).
45. Guo, L.; Zhu, C.; Xie, W.; Xu, F.; Wu, H.; Wan, Y.; Wang, Z.; Zhang, W.; Shen, J.; Wang, Z.B.; et al. Changjiang Delta in the Anthropocene: Multi-scale hydro-morphodynamics and management challenges. *Earth Sci. Rev.* **2021**, *223*, 103850. [CrossRef]
46. Vos, K.; Splinter, K.D.; Harley, M.D.; Simmons, J.A.; Turner, I.L. CoastSat: A Google Earth Engine-Enabled Python Toolkit to Extract Shorelines from Publicly Available Satellite Imagery. *Environ. Model. Softw.* **2019**, *122*, 104528. [CrossRef]
47. Sentinel-2 User Handbook. Available online: https://sentinel.esa.int/documents/247904/685211/Sentinel-2_User_Handbook (accessed on 31 December 2023).
48. Landsat 8 Data Users Handbook. Available online: https://www.usgs.gov/media/files/landsat-8-data-users-handbook (accessed on 31 December 2023).
49. Claverie, M.; Ju, J.; Masek, J.G.; Dungan, J.L.; Vermote, E.F.; Roger, J.-C.; Skakun, S.V.; Justice, C. The Harmonized Landsat and Sentinel-2 Surface Reflectance Data Set. *Remote Sens. Environ.* **2018**, *219*, 145–161. [CrossRef]
50. Vos, K.; Harley, M.D.; Splinter, K.D.; Simmons, J.A.; Turner, I.L. Sub-Annual to Multi-Decadal Shoreline Variability from Publicly Available Satellite Imagery. *Coast. Eng.* **2019**, *150*, 160–174. [CrossRef]

51. Nanson, R.; Bishop-Taylor, R.; Sagar, S.; Lymburner, L. Geomorphic Insights into Australia's Coastal Change Using a National Dataset Derived from the Multi-Decadal Landsat Archive. *Estuar. Coast. Shelf Sci.* **2022**, *265*, 107712. [CrossRef]
52. Cipolletti, M.P.; Delrieux, C.A.; Perillo, G.M.E.; Cintia Piccolo, M. Superresolution Border Segmentation and Measurement in Remote Sensing Images. *Comput. Geosci.* **2012**, *40*, 87–96. [CrossRef]
53. Vos, K.; Harley, M.D.; Splinter, K.D.; Walker, A.; Turner, I.L. Beach Slopes From Satellite-Derived Shorelines. *Geophys. Res. Lett.* **2020**, *47*, e2020GL088365. [CrossRef]
54. Yuan, R.; Zhang, H.; Qiu, C.; Wang, Y.; Guo, X.; Wang, Y.; Chen, S. Mapping Morphodynamic Variabilities of a Meso-Tidal Flat in Shanghai Based on Satellite-Derived Data. *Remote Sens.* **2022**, *14*, 4123. [CrossRef]
55. Groeneveld, D.P.; Barz, D.D. Dixie Valley, Nevada Playa Bathymetry Constructed from Landsat TM Data. *J. Hydrol.* **2014**, *512*, 435–441. [CrossRef]
56. Pulwarty, R.; Sivakumar, M.V.K. Information systems in a changing climate: Early warnings and drought risk management. *Weather. Clim. Extremes* **2014**, *3*, 14–21. [CrossRef]
57. Zhu, J.R.; Wu, H.; Li, L.; Wang, B. Saltwater intrusion in the Changjiang Estuary in the extremely drought hydrological year. *J. East China Norm. Univ.* **2010**, *4*, 1–6.
58. Record Drought Gripped Much of the U.S. in 2022. Available online: https://www.noaa.gov/news/record-drought-gripped-much-of-us-in-2022 (accessed on 31 December 2023).
59. Bonaldo, D.; Bellafiore, D.; Ferrarin, C.; Ferretti, R.; Ricchi, A.; Sangelantoni, L.; Vitelletti, M.L. The summer 2022 drought: A taste of future climate for the Po valley (Italy)? *Reg. Environ. Chang.* **2023**, *23*, 1. [CrossRef]
60. Liu, S.; Wu, Y.; Xu, G.; Cheng, S.; Zhong, Y.; Zhang, Y. Characterizing the 2022 Extreme Drought Event over the Poyang Lake Basin Using Multiple Satellite Remote Sensing Observations and In Situ Data. *Remote Sens.* **2023**, *15*, 5125. [CrossRef]
61. Duan, A.; Zhong, Y.; Xu, G.; Yang, K.; Tian, B.; Wu, Y.; Hu, E. Quantifying the 2022 extreme drought in the Yangtze River Basin using GRACE-FO. *J. Hydrol.* **2024**, *630*, 130680. [CrossRef]
62. Xu, G.; Wu, Y.; Liu, S.; Cheng, S.; Zhang, Y.; Pan, Y.; Wang, L.; Dokuchits, E.; Nkwazema, O.C. How 2022 extreme drought influences the spatiotemporal variations of terrestrial water storage in the Yangtze River Catchment: Insights from GRACE-based drought severity index and in-situ measurements. *J. Hydrol.* **2023**, *626*, 130245. [CrossRef]